Geophysical Research Letters

RESEARCH LETTER
10.1029/2022GL101278

Key Points:

- An efficient 3-D forward and inverse model based on the temporal moment is developed to solve Maxwell's equations in random parameter fields
- Triggered lightning tomography yields an excellent subsurface electric conductivity spatial distribution in a basin of several kilometers
- Deep lightning rods in the subsurface improve vertical resolution and depth of investigation

Supporting Information:

Supporting Information may be found in the online version of this article.

Correspondence to:

T.-C. J. Yeh,
yeh@hwr.arizona.edu

Citation:

Wang, Y.-L., Yeh, T.-C. J., Liu, F., Wen, J.-C., Wang, W., & Hao, Y. (2022). Characterize basin-scale subsurface using rocket-triggered lightning. *Geophysical Research Letters*, *49*, e2022GL101278. https://doi.org/10.1029/2022GL101278

Received 29 SEP 2022
Accepted 18 NOV 2022

Characterize Basin-Scale Subsurface Using Rocket-Triggered Lightning

Yu-Li Wang[1], Tian-Chyi Jim Yeh[2], Fei Liu[3], Jet-Chau Wen[4,5], Wenke Wang[6], and Yonghong Hao[7]

[1]Department of Bioenvironmental Systems Engineering, National Taiwan University, Taipei, Taiwan, [2]Department of Hydrology and Atmospheric Sciences, The University of Arizona, Tucson, AZ, USA, [3]School of Water Conservancy and Hydropower, Hebei University of Engineering, Handan, China, [4]Department of Safety, Health, and Environmental Engineering, National Yunlin University of Science and Technology, Douliu, Taiwan, [5]Research Center for Soil and Water Resources and Natural Disaster Prevention, National Yunlin University of Science and Technology, Douliu, Taiwan, [6]Key Laboratory of Subsurface Hydrology and Ecological Effects in Arid Region, Chang'an University, Xi'an, China, [7]Tianjin Key Laboratory of Water Resources and Environment, Tianjin Normal University, Tianjin, China

Abstract This paper exploits triggered lightning as a point source for the basin-scale electromagnetic tomographic survey to image 3-D subsurface electrical properties in basins. This paper further develops a new temporal moment approach, overcoming the difficulties in forward and inverse modeling of 3-D Maxwell's equations with heterogeneous parameter fields. Using this approach, we find that the influence of a single triggered lightning strike covers a radius of 20–70 km with detectable signals. The cross-correlation analysis between the moment difference of the electric and electric/magnetic property field indicates that the approach is suitable for mapping subsurface electric conductivity (σ) heterogeneity. A numerical experiment with 3-D spatially random parameter fields demonstrates that the method captures the spatial distribution of electric conductivity over large areas with a sparse monitoring network. It reveals the potential of using triggered lightning as a basin-scale electric/magnetic tomography survey.

Plain Language Summary Triggered lightning experiments traditionally aim at adverse impacts of lightning phenomena on near-surface structures (such as buildings, power, communication, and transportation networks). Magnetotellurics surveys have exploited electromagnetic (EM) waves from thunderstorm activities and the interaction of solar wind with the Earth's magnetosphere to map the subsurface structure, assuming that electromagnetic waves are planar and propagate vertically into the Earth. This paper, in contrast, explores the EM waves generated by flashes of lightning triggered by a lightning rocket at designated locations as EM point sources and their measurements at different depths and distances in the subsurface. Such experiments are tantamount to an EM tomographic survey, viewing the subsurface from different perspectives. This paper further develops a new stochastic methodology to analyze the propagation of EM waves in heterogeneous geologic media over hundreds of kilometers. These accomplishments permit harvesting the lightning signals to image the subsurface over greater depths and areas and address the image's uncertainty. Numerical experiments confirm the robustness of this proposed concept, which could be a new technology to explore subsurface processes and natural resources in basins and mountain terrains.

1. Introduction

Knowledge of detailed spatial distributions of geological structures is imperative to understanding the Earth's subsurface processes and exploring natural resources. Over the past decades, electrical magnetic (EM) surveys have been developed based on airborne, controlled-source, or natural-source methods (e.g., Magnetotellurics (MT) and Audio-frequency MT (AMT)). They have been valuable tools for studying hydrogeological features such as wetlands (McLachlan et al., 2021), aquifers (Koganti et al., 2020; Korus, 2018), volcanoes and geothermal areas (Árnason et al., 2010), hydrocarbon reservoirs (He et al., 2010; Mansoori et al., 2016), ore deposits (Tuncer et al., 2006), salinity mapping (Cox et al., 2012), and fault systems (Tietze & Ritter, 2013). Generally, the artificial EM surveys are suitable for shallow depths and small areas, while the MT yields general locations of anomalies at depth with little detail. High-resolution characterization of deep subsurface over large basins and mountain ranges remains challenging. This work exploits the available rocket-triggered lightning technology to tackle this challenge.

The proposed rocket-triggered lightning tomography exploits the enormous power of triggered lightning strikes (e.g., 300 million Volts and about 30,000 Amps, Li et al., 2019) at a specific location and depth in the subsurface, records the strike's energy, and monitors the EM signals at various locations and depths over a basin. These recorded signals are tantamount to snapshots of the subsurface heterogeneity at different perspectives (tomography), different from the traditional MT or AMT. Synthesizing these snapshots yields a three-dimensional image of the subsurface.

The interpretation of EM surveys requires forward and inverse analyses of EM wave propagation, which often faces issues related to numerical accuracy and computational costs (i.e., time and required resources). These issues are especially crucial in the lightning application because the measured potentials from lightning strikes have more complex waveforms than the instantaneous direct current resistivity. Analytical and numerical solutions to Maxwell's equations are available to study the propagation of EM waves in various spaces. Analytic solutions are limited to EM waves propagating through a simplified or specific geometric symmetry structure (Shvartsburg & Maradudin, 2013). They are valuable but do not yield information at the scale of our interest.

Forward numerical solutions are ideal for analyses of multidimensional and complex problems but often encounter other difficulties. For example, Yee (1966) developed a model using a rectangular grid and low-order finite difference discretizations. Such an approach often leads to enormous computation time for systems containing curved surfaces and material interfaces, although various improved algorithms are available (e.g., Ernst et al., 2007; Lee & Fornberg, 2003; Meles et al., 2010; Zheng et al., 1999). Likewise, many numerical EM inverse models have been developed (e.g., Egbert & Kelbert, 2012; Haber et al., 2004; Kelbert et al., 2014; Oldenburg et al., 2005; Pankratov & Kuvshinov, 2010). They again encountered colossal CPU time, even though adapting an adjoint approach and parallel computing. As a result, they are suitable for low-dimensional problems and depict general locations of anomalies (Newman & Alumbaugh, 1997, 2000; Newman & Boggs, 2004; Newman & Hoversten, 2000; Newman et al., 2003). For these reasons, a computationally efficient and versatile inverse numerical approach is highly desirable.

Recognizing the above difficulties, Lee and Xie (1993) developed a cross-hole EM travel time tomography, assuming the wave travel along a 1-D path to avoid the heavy computational burden required in EM inversion. This method employed low-frequency EM fields to reduce Maxwell's equation to a diffusion equation. Afterward, the diffusive EM fields are transformed into wavefields, and a 2-D conductivity image between the boreholes can be derived with little computational cost. Subsequently, Lee and Uchida (2005) applied EM travel time tomography for reservoir characterization in a small field site to demonstrate its usefulness and advantages.

The temporal moment method (Aris, 1958) has been applied to diffusion and advection-diffusion equations to delineate the structure of the subsurface (i.e., Cirpka & Kitanidis, 2000; Harvey & Gorelick, 1995; James et al., 1997; Jawitz et al., 2003; Jin et al., 1995; Leube et al., 2012; Valocchi, 1986; Yin & Illman, 2009; Zhu & Yeh, 2006). These works demonstrated that the approach significantly reduces computational costs while maintaining estimates' accuracy.

Here, we apply the moment method to Maxwell's equation to reduce the computational complexity of modeling EM wave propagation through 3-D randomly distributed electrical permeability and dielectric conductivity fields. Besides, we adopt the widely used stochastic successive linear estimator (SLE) for hydraulic tomography (Xiang et al., 2009; Yeh & Liu, 2000; Yeh et al., 1996) to estimate the most likely electrical property fields and to address their uncertainty in the proposed triggered lightning tomography.

As a proof-of-concept study, our objectives are (a) to explore the feasibility of utilizing electromagnetic responses induced by triggered lightning strikes to enhance subsurface characterization over a large-scale basin, (b) to evaluate the computational improvement of inverting EM signals using the temporal moment technique coupled with a stochastic estimator, and (c) to assess the ability of the technique for estimating different parameters. This paper first formulates the equations that govern EM propagation using temporal moments. It then demonstrates the feasibility of the temporal moments of rocket-triggered lightning tomography in a 3-D synthetic geological medium with randomly distributed parameters. Finally, we elucidate temporal moments' effectiveness in estimating the spatial distributed electrical properties using the cross-correlation analysis.

2. Methodology

2.1. Maxwell's Equations

Consider that an instantaneous current or rocket-triggered lightning strike transmits into the subsurface. The propagation of the EM field can be described by

$$\nabla \cdot \varepsilon \mathbf{E} = \rho \tag{1}$$

$$\nabla \cdot \mu \mathbf{H} = 0 \tag{2}$$

$$\nabla \times \mathbf{E} = -\frac{\partial \mu \mathbf{H}}{\partial t} \tag{3}$$

$$\nabla \times \mathbf{H} = \sigma \mathbf{E} + \frac{\partial \varepsilon \mathbf{E}}{\partial t} \tag{4}$$

where $\mathbf{E}$ is the electric field (Volt/L), $\mathbf{H}$ is the magnetic field (Amp/L), ε is the electrical permeability (Farad/L), μ is the magnetic permeability (Henry/L), σ is the electric conductivity (Siemens/L), ρ is the electric charge density (Coulomb/L^3), and t is time (T).

2.2. Temporal Moments of Maxwell's Equations

Solving the multidimensional Maxwell's equations is challenging even without considering spatially variable parameter fields. This paper proposes a temporal moment technique to overcome the difficulties.

Consider μ, ε, and σ are independent with time. Multiplying Equations 1–4 with time to its power n and integrating them over time, we have

$$\nabla \cdot \varepsilon \mathbf{M}_{\mathbf{E},n} = \int \rho t^n dt \tag{5}$$

$$\nabla \cdot \mu \mathbf{M}_{\mathbf{H},n} = 0 \tag{6}$$

$$\nabla \times \mathbf{M}_{\mathbf{E},n} = n\mu \mathbf{M}_{\mathbf{H},n-1} \tag{7}$$

$$\nabla \times \mathbf{M}_{\mathbf{H},n} = -n\varepsilon \mathbf{M}_{\mathbf{E},n-1} + \sigma \mathbf{M}_{\mathbf{E},n} \tag{8}$$

in which $\mathbf{M}$ is the temporal moments of $\mathbf{E}$ and $\mathbf{H}$ fields expressed as

$$\begin{aligned} \mathbf{M}_{\mathbf{E},n} &= \int \mathbf{E} t^n dt \\ \mathbf{M}_{\mathbf{H},n} &= \int \mathbf{H} t^n dt \end{aligned} \tag{9}$$

and n is any integer greater than or equal to zero.

Taking the curl on both sides of Equation 7, we have

$$\nabla \times (\nabla \times \mathbf{M}_{\mathbf{E},n}) = n\nabla \times (\mu \mathbf{M}_{\mathbf{H},n-1}) \tag{10}$$

Because $\nabla \times (\nabla \times \mathbf{M}_{\mathbf{E},n}) = \nabla (\nabla \cdot \mathbf{M}_{\mathbf{E},n}) - \nabla^2 \mathbf{M}_{\mathbf{E},n}$, Equation 10 becomes

$$\nabla (\nabla \cdot \mathbf{M}_{\mathbf{E},n}) - \nabla^2 \mathbf{M}_{\mathbf{E},n} = n\nabla \times (\mu \mathbf{M}_{\mathbf{H},n-1}) \tag{11}$$

Assuming μ is spatially uniform (or small variability) and substituting Equation 8 into Equation 11, we have

$$\nabla (\nabla \cdot \mathbf{M}_{\mathbf{E},n}) - \nabla^2 \mathbf{M}_{\mathbf{E},n} = n\mu\sigma \mathbf{M}_{\mathbf{E},n-1} - n(n-1)\mu\varepsilon \mathbf{M}_{\mathbf{E},n-2} \tag{12}$$

We further assume the spatial variability of ε is smaller than that of $\mathbf{M}_\mathbf{E}$. Thus, the divergence of $\mathbf{M}_\mathbf{E}$ is equal to zero (i.e., $\nabla \cdot \mathbf{M}_{\mathbf{E},n} = 0$) and Equation 12 becomes

$$-\nabla^2 \mathbf{M}_{\mathbf{E},n} = n\mu\sigma \mathbf{M}_{\mathbf{E},n-1} - n(n-1)\mu\varepsilon \mathbf{M}_{\mathbf{E},n-2} \tag{13}$$

The boundary condition is

$$\mathbf{M}_{\mathbf{E},n} = \int \mathbf{E}(t)t^n dt \tag{14}$$

Each coordinate axis component of $\mathbf{M}_{\mathbf{E}}$ satisfies a scalar Poisson's equation. That is,

$$-\nabla^2 M_{\mathbf{E}i,n} = n\mu\sigma M_{\mathbf{E}i,n-1} - n(n-1)\mu\varepsilon M_{\mathbf{E}i,n-2} \tag{15}$$

where $i = x$, y, or z. The boundary condition is

$$M_{\mathbf{E}i,n} = \int \mathbf{E}_i(t)t^n dt \tag{16}$$

Now Maxwell's equations are reduced to Poisson's equation. The temporal moments of the electric field are independent of the magnetic field and the time. For these reasons, difficulties associated with simulating the electromagnetic field in a randomly heterogeneous domain and boundary effects are avoided. This approach further eliminates the need for refining the mesh near the material interfaces to precisely capture the propagation of transmitted and reflected electromagnetic fields. The derivatives of the zeroth-, first-, and second-order moments are available in Supporting Information S1.

2.3. Cross-Correlations Between Temporal Moments and EM Parameters

Our proposed parameter estimation approach utilizing the stochastic cross-correlations between parameters and temporal moments is described next. The correlation uses a first-order approximation of the relationship between measurements of subsurface responses at a given location to the parameters at different locations. The first-order analysis is popular for examining highly nonlinear problems in groundwater hydrology (e.g., Gelhar, 1993), which requires evaluation of the sensitivity of the response of processes to parameters. An adjoint state approach (e.g., Sun & Yeh, 1990; Sykes et al., 1985) is adopted here to determine the sensitivity matrix of nth order temporal moments to parameters σ and ε. The approach's computational efficiency has been proven in many real-world applications of hydraulic tomography (Cardiff et al., 2020; Wang et al., 2022; Zha et al., 2016; Zhao & Illman, 2022).

Compared with the conventional time-domain finite difference approach, the temporal moment adjoint approach speeds up the correlation analysis. Consider that the electric fields are recorded from five receivers during two impulse excitations at a heterogeneous medium. The medium is discretized into 100 zones. The conventional time-domain finite difference approach requires solving (100 + 1)*2 = 202 time-marching Maxwell's equations to derive the sensitivity. On the other hand, the temporal moment adjoint approach only requires solving the time-independent adjoint Equation 5 times, which is significantly efficient. Detailed discussions are available in Supporting Information S1.

2.4. Inverse Algorithm

The SLE (Yeh et al., 1996), widely used in hydrogeology, is employed to estimate the parameters. The SLE is a geostatistical inverse approach that conceptualizes the parameter fields as spatial stochastic fields with a joint Gaussian distribution. They are characterized by means, variances, and 3-D exponential correlation structures in which correlation scales represent the statistically average length, width, and thickness of the geologic heterogeneity in the domain. The SLE then seeks the effective parameter fields conditioned on (or conformed to) the available measurements (e.g., nth temporal moments of the electric field) and addresses the uncertainty associated with the estimates. Detailed descriptions are available in Supporting Information S1.

2.5. Numerical Experiments

The synthetic numerical experiment mimics the subsurface structure beneath the Heilonggang plain, an important agricultural region located in the North China Plain in China. The synthetic subsurface structure follows the statistical characteristics of the area based on previous investigations (Zhou, 2008). A 3-D domain (260 km × 260 km × 40 km) is discretized using a variable grid (the grid sizes are between 2 and 40 km), resulting

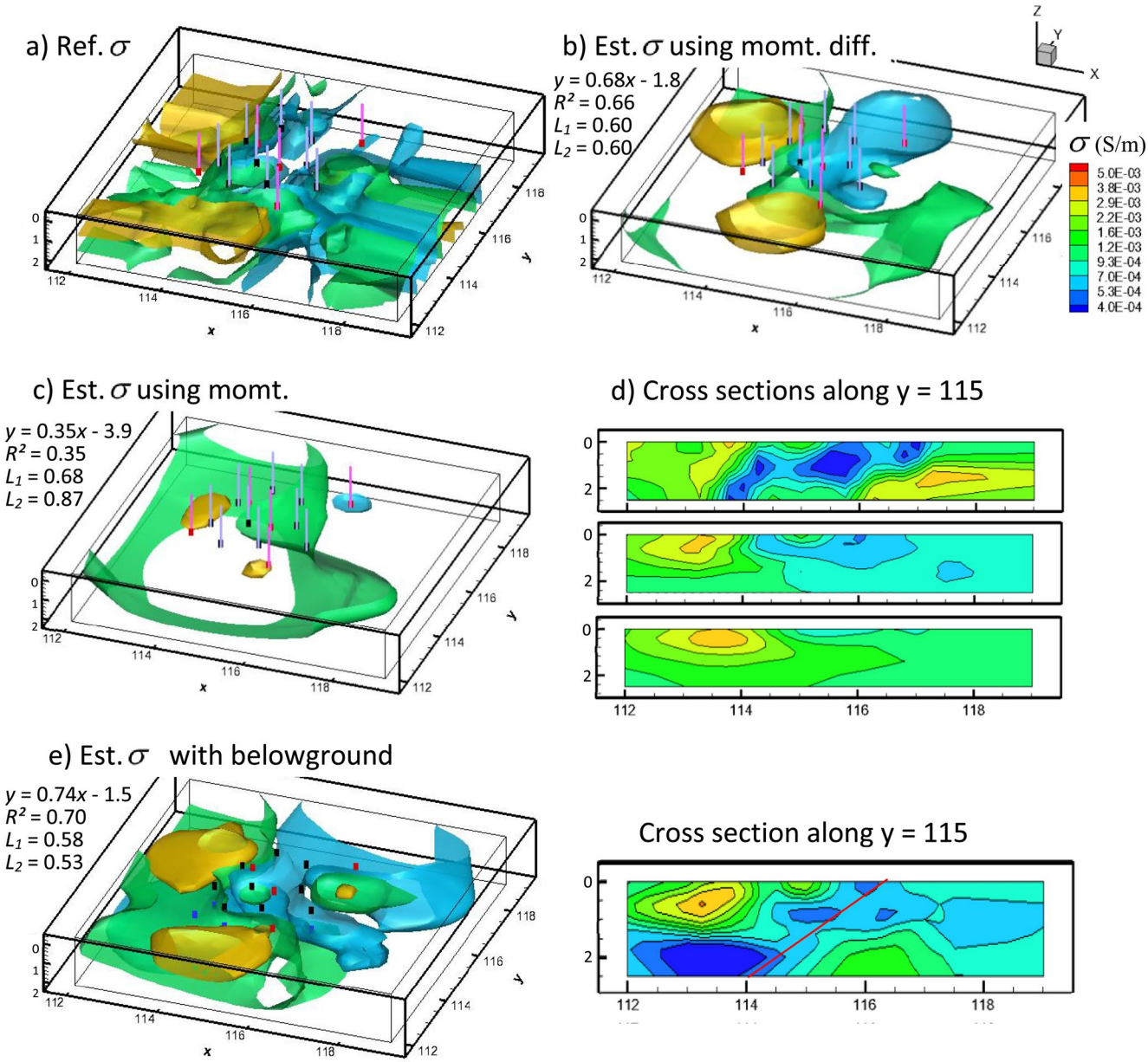

Figure 1. (a) The reference σ field. (b) The estimated σ using the moment difference. (c) The estimated σ using the moment. (d) The cross-section of the reference and estimate σ in (a–c). (e) The estimated σ field using the surface and belowground transmitters. In practice, the belowground transmitter can be placed in the tunnel, mountain front, or even the mountain valley. Only estimates whose uncertainty reduce 50% are used to calculate the best fit, R^2, and L_1 and L_2 norms metrics. The scatterplots comparing the estimated parameter with the reference case are available in Supporting Information S1 (Figure S3). The iso-surface levels are 0.0037 (yellow), 0.0012 (green), and 0.0006 (blue) S/m. The red dots represent transmitters placed on the ground surface, the black dots represent receivers placed on the ground surface, and the blue dots represent the belowground transmitters. The vertical purple and pink lines are used to better illustrate the relative positions of transmitters and receivers. The units of x, y, and z directions are km. The red line is the location of dike (blue color).

in a total of 30 × 30 × 20 elements. Each element is 0.25 km × 0.25 km × 0.2 km in the center of the domain. A zero electric field boundary bounds the subsurface. The land surface and bottom of the domain are no flux boundaries. Two heterogeneous reference fields (σ and ε) were generated using a spectral method. The reference σ field is displayed in Figure 1a, where the means of σ and ε were 1.3 S/km and 1.1×10^{-8} F/km. The variances of ln σ and ln ε were 0.5 and 0.2. The correlation lengths in the x, y, and z directions were 0.8, 0.8, and 0.6 km. These parameters are selected based on the available geological information (Wang et al., 2020). These initial guesses are soft constraints and will be updated by fusing the information embedded in observations at each iteration of SLE. Therefore, the estimated parameter fields are not fully sensitive to these initial guesses (Liu et al., 2020;

Tso et al., 2016). An instantaneous current is introduced to a selected transmitting electrode (red in Figure 1). The other electrodes and coils (black in Figure 1) then collect the electromagnetic response fields for the moment analysis. The same operation is performed sequentially at each electrode until all transmissions are completed. Due to inherent numerical difficulties in solving Maxwell's equations for such a heterogeneous parameter field using the traditional numerical approach, the moments are simulated using the temporal moment equations. A 3% noise was added to the observed moments to mimic the lumped effects of measurement, truncation, and integration errors.

Two types of measurements are utilized in the inversion. One is the moments and the other is the moment differences. The moment differences are gathered by subtracting the moments between two receivers. These inversions assume that the prior mean of σ is 0.1 S/km, the mean of ϵ is 10^{-8} F/km, the variances of ln σ and ln ϵ are 1, and the correlation length of each direction is 10, 10, and 0.4 km. The computation is implemented in a 3-D finite element model VSAFT3 (Yeh et al., 1993) to estimate σ and ϵ with the observed moments.

3. Results

3.1. Validation of the Moment Approach

The first step is to validate the temporal moment equations and their inverse solution using a simulated 2-D electromagnetic field in response to a point source at the center of the domain using COMSOL Multiphysics. Figure S1a in Supporting Information S1 shows a 180 km × 180 km domain composed of four homogeneous zones of different σ values (0.1, 0.01, 0.001, and 0.0001 S/m). An impulse of E field with Gaussian distribution (mean of 4 ms and standard deviation of 0.5 ms), mimicking that from a bolt of rocket-triggered lightning, is assumed as the source. The boundary conditions are zero E, and the initial conditions are zero E and H fields. Afterward, Simpson's rule is applied to calculate the electric field's zeroth and first temporal moments. These temporal moment values along the radius centered at the source point are compared with the values directly simulated by the temporal moment equations (Equations 15 and 16). The scatterplots of the zeroth and first moments (Figures S1b and S1c in Supporting Information S1) verify the temporal moment derivations. The first moment values are slightly scattered along the 45° line attributed to errors from the integration using the trapezoidal rule. After the validation, these first moments from Simpson's rule are utilized to estimate the σ values. The estimated σ converges to the actual values (Figure S1d in Supporting Information S1), confirming the reliability and validity of the inverse algorithm.

3.2. Area of Influence

We next evaluate how far, deep, and fast a strike can propagate through a lossy subsurface geological medium. Suppose the μ, σ, and ϵ are spatially uniform, Maxwell's equations reduce to the scalar wave equation

$$\nabla^2 E = \sigma\mu\frac{\partial E}{\partial t} + \mu\epsilon\frac{\partial^2 E}{\partial t^2} \tag{17}$$

$$\nabla^2 H = \sigma\mu\frac{\partial H}{\partial t} + \mu\epsilon\frac{\partial^2 H}{\partial t^2} \tag{18}$$

where $1/\sqrt{\mu\epsilon}$ is the speed of the wavefront. The μ values of non-ferromagnetic materials are almost identical to that of vacuum. The ϵ values of rock and soil are around 2 to 50 times greater than that of vacuum. Thus, the speed of a lightning strike propagating through a lossy medium is 2–7 times slower than the speed of light (i.e., 40,000–150,000 km/s), indicating that existing technology can accurately capture the signal.

The zeroth moment (Equation S3 in Supporting Information S1) represents the amount of E passing through a given location. The values should be greater than a given tolerance (e.g., ambient E field variations and self-potential (SP) temporal variations). The temporal SP variation can be ignored because the time scale of SP changes due to the variations of hydrological and climate conditions are much longer than the lightning-triggered E field variations (>1 Hz). The ambient E field induced by the nearby wire, electronic devices, and base stations in a typical residential area is about several tens of volts per meter. In addition, most electric power is operated under 50–60 Hz. Effects of anthropogenic E field can therefore be easily removed.

Consider an infinite homogeneous half-sphere with a point source (Figure S2a in Supporting Information S1) on the ground surface. The ground boundary is no flux. The μ value is 10^{-6} H/m, and the ϵ value is 10^{-11} H/m. The four different σ values, 10^{-1}, 10^{-2}, 10^{-3}, and 10^{-4} S/m for most geologic media, are investigated. Figure S2b in Supporting Information S1 illustrates the maximum E values at different radio distances from the location of the current injection. It shows that when the σ value is 10^{-4} S/m, the maximum E values at 100 km away from the stroke location are greater than 1 V/m. Even in the worst scenario, where σ value is 10^{-1} S/m, a reasonably large E value (0.1 V/m) can still be detected from 20 km. This analysis proves the feasibility of exploiting triggered lightning for characterizing large-scale geologic basins using the proposed tomography survey.

3.3. Estimated σ and ϵ Fields

Figure 1 compares the reference field (Figure 1a) with the estimated σ field based on the measurements of the temporal moment difference between pairs of receivers (Figure 1b) and the measurements of the temporal moments at a receiver (Figure 1c). The transmitters and receivers are installed on the ground surface in these cases. These figures show that the estimates from both moment measurements reveal the general pattern of spatial variation. However, the pattern from the temporal moments is smoother than the field from the moment differences measurements. Figure 1d compares the cross sections of the reference σ field (upper figure) with those in Figure 1b (middle figure) and Figure 1c (bottom figure). We notice that the stratifications and heterogeneity along the vertical direction are resolved using the moment difference. The spatial distributions of ϵ fields in these two approaches are almost uniform across the entire field.

Next, we demonstrate that emitting the triggered lightning strike via deep underground lightning rods benefits the subsurface characterization. Figure 1e illustrates the estimated σ 3-D field (left figure) and a cross-section (right figure) using transmitters on the ground surface (red dots) and at 1 km belowground (blue dots), while the receivers are on the ground (black dots). In practice, the belowground transmitter can be placed in the tunnel, mountain front, or even the mountain valley. A comparison of σ fields in Figures 1b, 1c, and 1e reveals that the additional belowground transmitters profoundly improve the vertical resolution of estimate at deeper subsurface. The dike structure (the blue color region along the solid red line) and relatively high σ zone (the green color at 2 km depth) are captured, while they are not visible in the case where the surface transmitters were used. The scatterplots comparing the estimated parameter with the reference case are available in Supporting Information S1 (Figure S3).

4. Discussions

4.1. The Role of Observed Moment in Inversion

To explain our approach's ability to estimate different parameters, we calculate the spatial cross-correlations between the temporal moment of a signal observed at a location and electromagnetic parameters at different locations. The spatial correlation reveals the most likely location where a unit variation in σ or ϵ contributes the most to the variation of the electromagnetic response at a given location. These correlations are evaluated at the mean electrical properties (the mean values of σ and ϵ are 10^{-1} S/km and 10^{-8} F/km, and the correlation lengths are 10, 10, and 5 km along x, y, and z directions). The subsurface is bounded by a constant moment boundary (electric field = 0). A source (triangles in Figure 2) is placed at the center of the domain, and a receiver (circle in Figure 2) is at 15 km away from the source.

Figure 2a illustrates the cross-correlation between the first moment and σ, while Figure 2b is that between the second moment and ϵ. Notice that the zeroth moment does not depend on both parameters, and the first moment is independent of ϵ (see Equations S3 and S5 in Supporting Information S1). We observed that the first moment at the receiver location is positively correlated with the σ everywhere (Figure 2a), highest in the region between the source and receiver, and gradually decreases toward the boundary. A positive correlation means that if the observed moment at the receiver is greater than the calculated moment based on the mean σ value, the actual σ values at the positive correlation locations are likely greater than the mean.

On the other hand, the second moment is negatively correlated with ϵ everywhere (Figure 2b), with the highest correlation in the region between the source and receiver. The cross-correlation distributions are similar in Figures 2a and 2b. However, the signs are opposite, and the absolute values of correlation between moment and

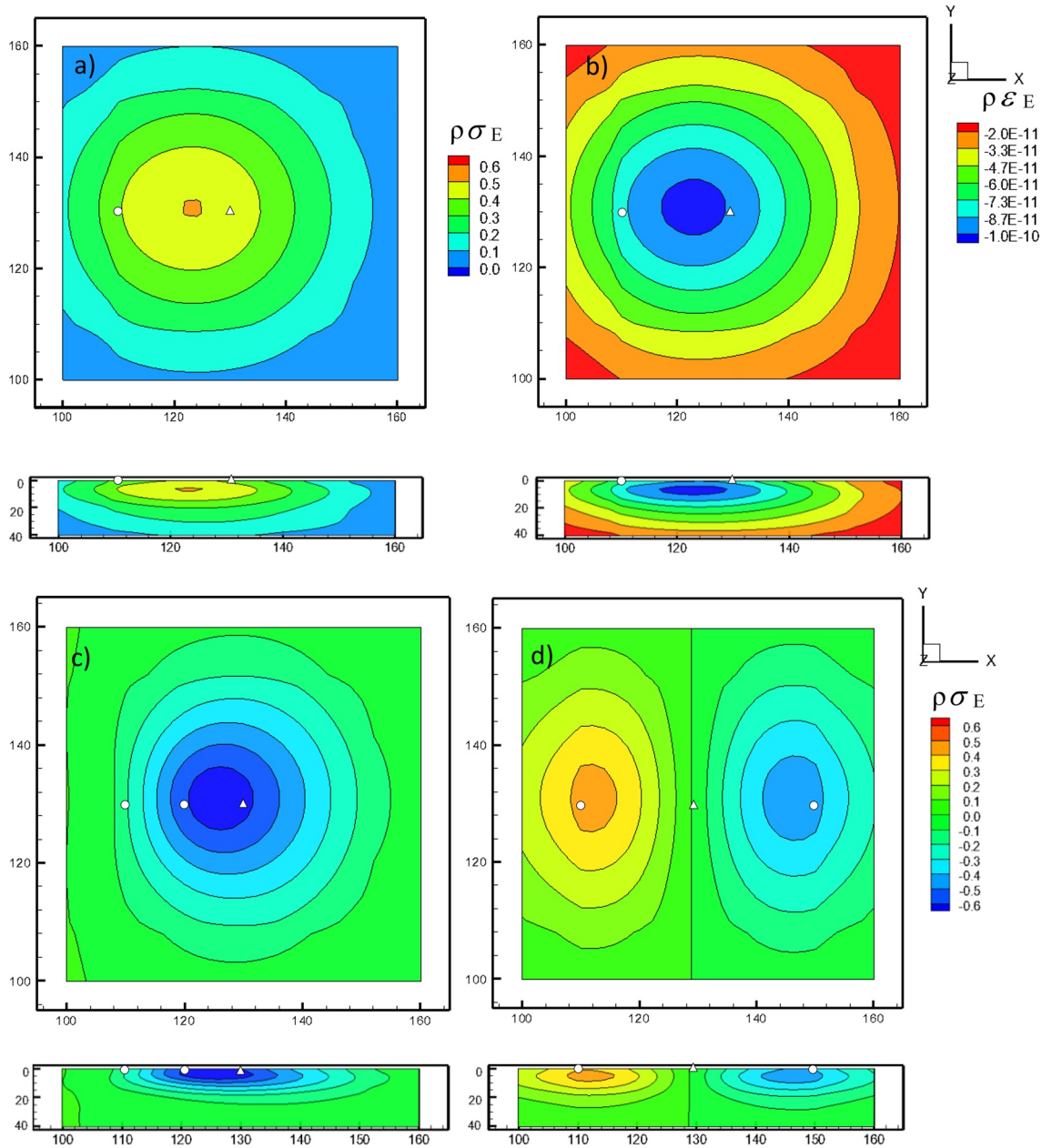

Figure 2. The upper row is correlations of $\mathbf{M}_{\mathbf{E},n}$ with respect to ln σ and ln ε. The bottom row is the correlation of $\mathbf{M}_{\mathbf{E},n}$ difference between the two receivers with respect to ln σ and ln ε. The sources and receivers are deployed on the ground surface. The triangles represent transmitters, and the circles represent receivers. The units of x, y, and z directions are km.

ε are profoundly smaller than that between moment and σ (around 10 orders smaller). That says an accurate estimation of ε property is unlikely.

Consider a different source and receiver pair (e.g., a north-south pair perpendicular to the east-west pair). The high correlation values remain in the source and receiver pair region due to the concentric-circle-shape cross-correlation distribution (similar to Figures 2a and 2b). This similarity indicates that including measurements collected from this additional source and receiver pair does not provide new information to infer other possible anomaly and heterogeneity locations.

Our new approach that uses the difference in moments at different pairs of receivers based on the same source location overcomes this issue. Figures 2c and 2d illustrate the correlations of the moment difference for σ using

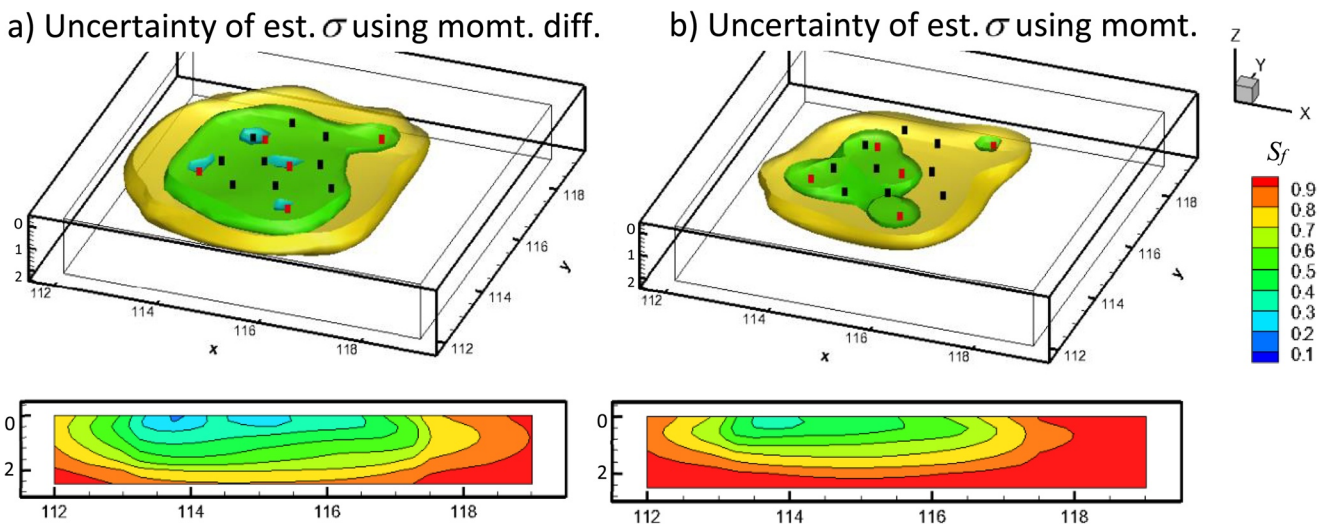

Figure 3. The uncertainty maps of estimated σ using (a) moment difference and (b) moment. The red lines represent transmitters and the black lines represent receivers. The cross sections are along $y = 115$. The iso-surface levels are 0.76 (yellow), 0.53 (green), and 0.29 (blue). The units of x, y, and z directions are km.

different pairs of receivers. A comparison between Figures 2c and 2d indicates that the high correlation values cover various areas. The moment difference negatively correlates with the area concentrated between the source and receiver pair if the receivers are placed on the same side of the source (Figure 2c). On the other hand, the moment difference is less correlated with σ in the area between the source and receiver pair if the receivers are placed on both sides of the source (Figure 2d). The spatial distribution is a dumbbell shape where the high correlation values are located in the regions away from the source. The correlation shapes in Figures 2c and 2d indicate that different combinations of a source and two receivers are beneficial to pinpoint the most likely anomaly and heterogeneity locations. Because of this reason, the estimated σ distributions using moment difference (Figure 1b) are superior to the estimate using moment (Figure 1c).

The spatial patterns of the correlation between the temporal moment difference and ε are similar to that of σ but with an opposite sign. Similar to the correlation values in Figure 2b, the absolute values of correlation are profoundly smaller than the correlation with σ (around 10 orders smaller). The small correlation value reveals that ε anomaly does not contribute significantly to the spatial variation of the moment. Because σ dominates the moment spatial distribution, the ε spatial distribution is difficult to estimate.

A stochastic uncertainty index, $\mathbf{S}_f(n \times 1)$, can further explain the benefit of using moment difference and is defined as

$$\mathbf{S}_f^{(\text{last})} = \frac{\text{dia}\left[\boldsymbol{\varepsilon}_{\text{ff}}^{(\text{last})}\right]}{\text{dia}\left[\boldsymbol{\varepsilon}_{\text{ff}}^{(0)}\right]} \tag{19}$$

in which $\boldsymbol{\varepsilon}_{\text{ff}}^{(\text{last})}$ is the residual covariance matrix of the last iteration from Equation S16 in Supporting Information S1, $\boldsymbol{\varepsilon}_{\text{ff}}^{(0)}$ is the prior covariance matrix at iteration zero, and dia[·] represents the diagonal term. This index is the residual variance at the last iteration of SLE normalized by the prior uncertainty due to unresolved heterogeneity. It represents the uncertainty of the estimated parameter after including temporal moment or temporal moment difference measurements at the receivers. A small value of $\mathbf{S}_f$ at a location means that the estimate's uncertainty is small, indicative of the measurements' effectiveness. On the contrary, if the $\mathbf{S}_f$ value is close to one, the uncertainty is not reduced after including the measured information (the information is ineffective).

The uncertainty maps in Figure 3 correspond to the estimates using different forms of measurements (Figures 1b and 1c). A comparison of the maps reveals that the distribution of small uncertainty (green color) covers broader regions in Figure 3a than those in Figure 3b. Such a difference implies that the temporal moment difference contains more information about the subsurface heterogeneity than the temporal moment measurement, corroborating with the cross-correlation analysis.

4.2. Differences With Travel Time Tomography

Many have applied artificially generated EM waves in a tomographic fashion to infer the cross-sectional parameter distributions between two boreholes (e.g., Lee & Xie, 1993). Their interpretation assumes the wave propagates in one dimension and is modified by the subsurface properties along the 1-D pathway between each source and receiver pair. It also inherently omits the effects of heterogeneities outside the 1-D wave propagation pathway. Consequently, this approach requires densely distributed sources and receivers to capture 3-D anomalies. In contrast, the proposed temporal moment approach accounts for the effects of 3-D heterogeneity as the wave propagates.

Besides, EM travel time tomography ignores the refraction and reflection of EM fields along the boundaries between different zones. Its trajectory-based formulations of arrival time also relied upon an asymptotic approach that assumes smoothly varying properties compared to the length scale associated with the propagating EM transient (Vasco & Datta-Gupta, 2016; Vasco et al., 2000). Such an assumption is not likely valid in the layered sedimentary environments and the subsurface with faults or fractures. On the other hand, the temporal moment approach is free of this limitation and suitable for heterogeneous subsurface environments.

Finally, the EM travel time tomography further minimizes the influence of electrical permeability ϵ by employing the low-frequency EM fields (<1 MHz) even though the spatial variation of ϵ plays a minor role in the EM field propagation. Despite these issues, the travel time approach is a simple and practical tool for a first-cut analysis providing a piece of prior information for a fully 3D inversion.

5. Conclusions

This study proposes the triggered lightning tomographic survey for basin-scale subsurface characterization. A 3-D numerical experiment and cross-correlation analysis confirm the effectiveness of this approach. The approach can serve as a viable tool for delineating the multidimensional and random electromagnetic properties over tens of kilometers.

The proposed temporal moment approach significantly reduces the computational difficulty. It transforms Maxwell's equations to Poisson's equation, decouples the interaction between the electrical and magnetic fields, and avoids the need for extremely fine spatial and temporal discretizations. The temporal integration also avoids the time-marching operation. The significant reduction in the computational effort on the forward solution and sensitivity analysis makes the inverse solution to Maxwell's equation for 3-D random parameter fields much more easily achievable.

This study also demonstrates that the spatial cross-correlation map of the temporal moment difference is more spatially variable than the temporal moment alone. Thus, the moment differences effectively reveal the most likely anomaly and heterogeneity locations.

Triggered lightning tomography is a potential new technology for scanning large-scale mountain range interiors. It may further lead to new lightning networks for monitoring the mountain range interior by exploiting the natural flashes of lightning as point sources through lighting rods installed deep in the mountain range or its valleys and peaks. These networks could continuously map natural resources and potential geohazards over the mountain terrain. Moreover, Fullea (2017) remarked that electrical conductivity and the primary rock properties describing the thermochemical state of rocks within the Earth (e.g., temperature, composition, melts) could be combined to enhance the interpretation and understanding of the subsurface. More detailed discussions of the benefits and challenges of joint inversion are available in Moorkamp (2017).

Finally, this study promotes adopting triggered lightning as point sources for basin-scale EM tomography. It develops the temporal moment approach to overcome the challenge of solving Maxwell's equations for the EM survey and a stochastic inverse approach to address the most likely estimates and their uncertainty. Nevertheless, the idea of triggered lightning tomography is still in the concept-developing stage. Many issues remain to be resolved, for example, (a) the assumption that magnetic permeability is uniform, (b) the SP and induced polarization effects are minor, and (c) a method to infer the spatial variability of electrical permeability is needed. Nevertheless, this study demonstrates that the triggered lightning experiment coupled with temporal moment analysis that reduces the computational burden in interpreting the tomographic datasets can yield reasonable estimates of the electric conductivity field, making a step toward applying it to real-world problems.

Data Availability Statement

The program and the data used in this study are available at https://doi.org/10.5281/zenodo.5214835.

Acknowledgments
We would like to acknowledge the support of the US NSF Grant EAR1931756 and TW NSC Grant MOST111-2222-E-002-006. The authors thank the editors and reviewers for their helpful and insightful comments, which have significantly improved this work.

References

Aris, R. (1958). On the dispersion of linear kinematic waves. *Proceedings of the Royal Society of London*, *A245*, 268–277. https://doi.org/10.1098/rspa.1958.0082

Árnason, K., Eysteinsson, H., & Hersir, G. P. (2010). Joint 1D inversion of TEM and MT data and 3D inversion of MT data in the Hengill area. SW Iceland. *Geothermics*, *39*(1), 13–34. https://doi.org/10.1016/j.geothermics.2010.01.002

Cardiff, M., Zhou, Y., Barrash, W., & Kitanidis, P. K. (2020). Aquifer imaging with oscillatory hydraulic tomography: Application at the field scale. *Ground Water*, *58*(5), 710–722. https://doi.org/10.1111/gwat.12960

Cirpka, O. A., & Kitanidis, P. K. (2000). Sensitivity of temporal moments calculated by the adjoint-state method and joint inversing of head and tracer data. *Advances in Water Resources*, *24*(1), 89–103. https://doi.org/10.1016/S0309-1708(00)00007-5

Cox, L. H., Wilson, G. A., & Zhdanov, M. S. (2012). 3D inversion of airborne electromagnetic data using a moving footprint. *Exploration Geophysics*, *41*(4), 250–259. https://doi.org/10.1071/EG10003

Egbert, G. D., & Kelbert, A. (2012). Computational recipes for electromagnetic inverse problems. *Geophysical Journal International*, *189*(1), 167–251. https://doi.org/10.1111/j.1365-246X.2011.05347.x

Ernst, J. R., Maurer, H., Green, A. G., & Holliger, K. (2007). Full-waveform inversion of crosshole radar data based on 2-D finite-difference time-domain solutions of Maxwell's equations. *IEEE Transactions on Geoscience and Remote Sensing*, *45*(9), 2807–2828. https://doi.org/10.1109/TGRS.2007.901048

Fullea, J. (2017). On joint modelling of electrical conductivity and other geophysical and petrological observables to infer the structure of the lithosphere and underlying upper mantle. *Surveys in Geophysics*, *38*(5), 963–1004. https://doi.org/10.1007/s10712-017-9432-4

Gelhar, L. W. (1993). *Stochastic subsurface hydrology* (p. 390). Prentice Hall. ISBN: 0138467676.

Haber, E., Ascher, U. M., & Oldenburg, D. W. (2004). Inversion of 3D electromagnetic data in frequency and time domain using an inexact all-at-once approach. *Geophysics*, *69*(5), 1216–1228. https://doi.org/10.1190/1.1801938

Harvey, C. F., & Gorelick, S. M. (1995). Temporal moment-generating equations: Modeling transport and mass transfer in heterogeneous aquifers. *Water Resources Research*, *31*(8), 1895–1911. https://doi.org/10.1029/95WR01231

He, Z., Hu, Z., Luo, W., & Wang, C. (2010). Mapping reservoirs based on resistivity and induced polarization derived from continuous 3D magnetotelluric profiling: Case study from Qaidam basin, China. *Geophysics*, *75*(1), B25–B33. https://doi.org/10.1190/1.3279125

James, A. I., Graham, W. D., Hatfield, K., Rao, P. S. C., & Annable, M. D. (1997). Optimal estimation of residual non–aqueous phase liquid saturations using partitioning tracer concentration data. *Water Resources Research*, *33*(12), 2621–2636. https://doi.org/10.1029/97WR02589

Jawitz, J. W., Annable, M. D., Demmy, G. G., & Rao, P. S. C. (2003). Estimating nonaqueous phase liquid spatial variability using partitioning tracer higher temporal moments. *Water Resources Research*, *39*(7), 1192. https://doi.org/10.1029/2002WR001309

Jin, M., Delshad, M., Dwarakanath, V., McKinney, D. C., Pope, G. A., Sepehrnoori, K., et al. (1995). Partitioning tracer test for detection, estimation, and remediation performance assessment of subsurface nonaqueous phase liquids. *Water Resources Research*, *31*(5), 1201–1211. https://doi.org/10.1029/95WR00174

Kelbert, A., Meqbel, N., Egbert, G. D., & Tandon, K. (2014). ModEM: A modular system for inversion of electromagnetic geophysical data. *Computers & Geosciences*, *66*, 40–53. https://doi.org/10.1016/j.cageo.2014.01.010

Koganti, T., Van De Vijver, E., Allred, B. J., Greve, M. H., Ringgaard, J., & Iversen, B. V. (2020). Mapping of agricultural subsurface drainage systems using a frequency-domain ground penetrating radar and evaluating its performance using a single-frequency multi-receiver electromagnetic induction instrument. *Sensors*, *20*(14), 3922. https://doi.org/10.3390/s20143922

Korus, J. (2018). Combining hydraulic head analysis with airborne electromagnetics to detect and map impermeable aquifer boundaries. *Water*, *10*(8), 975. https://doi.org/10.3390/w10080975

Lee, J., & Fornberg, B. (2003). A Split step Approach for the 3-D Maxwell's equations. *Journal of Computational and Applied Mathematics*, *158*(2), 485–505. https://doi.org/10.1016/S0377-0427(03)00484-9

Lee, K. H., & Xie, G. (1993). A new approach to imaging with low-frequency electromagnetic fields. *Geophysics*, *58*(6), 780–796. https://doi.org/10.1190/1.1443464

Lee, T. J., & Uchida, T. (2005). Electromagnetic traveltime tomography: Application for reservoir characterization in the Lost Hills oil field, California. *Geophysics*, *70*(3), G51–G58. https://doi.org/10.1190/1.1925743

Leube, P. C., Nowak, W., & Schneider, G. (2012). Temporal moments revisited: Why there is no better way for physically based model reduction in time. *Water Resources Research*, *48*(11), W11527. https://doi.org/10.1029/2012WR011973

Li, X., Lu, G., Fan, Y., Jiang, R., Zhang, H., Li, D., et al. (2019). Underground measurement of magnetic field pulses during the early stage of rocket-triggered lightning. *Journal of Geophysical Research: Atmospheres*, *124*(6), 3168–3179. https://doi.org/10.1029/2018JD029682

Liu, F., Yeh, T.-C., Wang, Y.-L., Hao, Y., Wen, J.-C., & Wang, W. (2020). Characterization of basin-scale aquifer heterogeneity using transient hydraulic tomography with aquifer responses induced by groundwater exploitation reduction. *Journal of Hydrology*, *588*, 125137. https://doi.org/10.1016/j.jhydrol.2020.125137

Mansoori, I., Oskooi, B., Pedersen, L., & Javaheri, R. (2016). Three-dimensional modelling of magnetotelluric data to image Sehqanat hydrocarbon reservoir in southwestern Iran. *Geophysical Prospecting*, *64*(3), 753–766. https://doi.org/10.1111/1365-2478.12328

McLachlan, P., Blanchy, G., Chambers, J., Sorensen, J., Uhlemann, S., Wilkinson, P., & Binley, A. (2021). The application of electromagnetic induction methods to reveal the hydrogeological structure of a riparian wetland. *Water Resources Research*, *57*(6), e2020WR029221. https://doi.org/10.1029/2020WR029221

Meles, G. A., Van der Kruk, J., Greenhalgh, S. A., Ernst, J. R., Maurer, H., & Green, A. G. (2010). A new vector waveform inversion algorithm for simultaneous updating of conductivity and permittivity parameters from combination crosshole/borehole-to-surface GPR data. *IEEE Transactions on Geoscience and Remote Sensing*, *48*(9), 3391–3407. https://doi.org/10.1109/TGRS.2010.2046670

Moorkamp, M. (2017). Integrating electromagnetic data with other geophysical observations for enhanced imaging of the Earth: A tutorial and review. *Surveys in Geophysics*, *38*(5), 935–962. https://doi.org/10.1007/s10712-017-9413-7

Newman, G. A., & Alumbaugh, D. L. (1997). Three-dimensional massively parallel electromagnetic inversion, I. Theory. *Geophysical Journal International*, *128*, 345–354. https://doi.org/10.1111/j.1365-246X.1997.tb01559.x

Newman, G. A., & Alumbaugh, D. L. (2000). Three-dimensional magnetotelluric inversion using non-linear conjugate gradients. *Geophysical Journal International*, *140*(2), 410–424. https://doi.org/10.1046/j.1365-246x.2000.00007.x

Newman, G. A., & Boggs, P. T. (2004). Solution accelerators for large-scale three-dimensional, electromagnetic inverse problems. *Inverse Problems*, *20*(6), 151–170. https://doi.org/10.1088/0266-5611/20/6/S10

Newman, G. A., & Hoversten, G. M. (2000). Solution strategies for two-and three- dimensional electromagnetic inverse problems. *Inverse Problems*, *16*(5), 1357–1375. https://doi.org/10.1088/0266-5611/16/5/314

Newman, G. A., Recher, S., Tezkan, B., & Neubauer, F. M. (2003). 3D inversion of a scalar radio magnetotelluric field dataset. *Geophysics*, *68*(3), 791–802. https://doi.org/10.1190/1.1581032

Oldenburg, D. W., Eso, R., Napier, S., & Haber, E. (2005). Controlled source electromagnetic inversion for resource exploration. *First Break*, *23*(7), 41–48. https://doi.org/10.3997/1365-2397.23.7.26611

Pankratov, O., & Kuvshinov, A. (2010). General formalism for the efficient calculation of derivatives of EM frequency-domain responses and derivatives of the misfit. *Geophysical Journal International*, *181*(1), 229–249. https://doi.org/10.1111/j.1365-246X.2009.04470.x

Shvartsburg, A. B., & Maradudin, A. A. (2013). *Waves in gradient metamaterials*. World Scientific Publication. https://doi.org/10.1142/8649

Sun, N.-Z., & Yeh, W.-W.-G. (1990). Coupled inverse problems in groundwater modeling: 1. Sensitivity analysis and parameter identification. *Water Resources Research*, *26*(10), 2507–2525. https://doi.org/10.1029/WR026i010p02507

Sykes, J. F., Wilson, J. L., & Andrews, R. W. (1985). Sensitivity analysis for steady-state groundwater flow using adjoint operators. *Water Resources Research*, *21*(3), 359–371. https://doi.org/10.1029/WR021i003p00359

Tietze, K., & Ritter, O. (2013). Three-dimensional magnetotelluric inversion in practice-the electrical conductivity structure of the San Andreas Fault in Central California. *Geophysical Journal International*, *195*(1), 130–147. https://doi.org/10.1093/gji/ggt234

Tso, C.-H. M., Zha, Y., Yeh, T.-C. J., & Wen, J.-C. (2016). The relative importance of head, flux, and prior information in hydraulic tomography analysis. *Water Resources Research*, *52*(1), 3–20. https://doi.org/10.1002/2015WR017191

Tuncer, V., Unsworth, M. J., Siripunvaraporn, W., & Craven, J. A. (2006). Exploration for unconformity-type uranium deposits with audi-omagnetotelluric data: A case study from the McArthur River mine, Saskatchewan. Canada. *Geophysics*, *71*(6), B201–B209. https://doi.org/10.1190/1.2348780

Valocchi, A. J. (1986). Effect of radial flow on deviations from local equilibrium during sorbing solute transport through homogeneous soils. *Water Resources Research*, *22*(12), 1693–1701. https://doi.org/10.1029/WR022i012p01693

Vasco, D., & Datta-Gupta, A. (2016). *Subsurface fluid flow and imaging: With applications for hydrology, reservoir engineering, and geophysics*. Cambridge University Press. https://doi.org/10.1017/CBO9781139018876

Vasco, D. W., Keers, H., & Karasaki, K. (2000). Estimation of reservoir properties using transient pressure data: An asymptotic approach. *Water Resources Research*, *36*(12), 3447–3465. https://doi.org/10.1029/2000WR900179

Wang, G.-L., Wang, W.-L., Zhang, W., Ma, F., & Liu, F. (2020). The status quo and prospect of geothermal resources exploration and development in Beijing-Tianjin-Hebei region in China. *China Geology*, *3*(1), 173–181. https://doi.org/10.31035/cg2020013

Wang, Y.-L., Chang, L.-C., Liu, F., Ho, Y.-T., Wang, T. B., Yeh, T.-C. J., & Tsai, J.-P. (2022). Aquifer characterization using fiber Bragg grating multi-level monitoring system. *Ground Water*, *60*(4), 518–529. https://doi.org/10.1111/gwat.13186

Xiang, J., Yeh, T.-C. J., Lee, C.-H., Hsu, K.-C., & Wen, J.-C. (2009). A simultaneous successive linear estimator and a guide for hydraulic tomography analysis. *Water Resources Research*, *45*(2), W02432. https://doi.org/10.1029/2008WR007180

Yee, K. S.-G. (1966). Numerical solution of initial boundary value problems involving Maxwell's equations in isotropic media. *IEEE Transactions on Antennas and Propagation*, *14*(3), 302–307. https://doi.org/10.1109/TAP.1966.1138693

Yeh, T.-C.-J., Jin, M., & Hanna, S. (1996). An iterative stochastic inverse method: Conditional effective transmissivity and hydraulic head fields. *Water Resources Research*, *32*(1), 85–92. https://doi.org/10.1029/95WR02869

Yeh, T.-C. J., & Liu, S. (2000). Hydraulic tomography: Development of a new aquifer test method. *Water Resources Research*, *36*(8), 2095–2105. https://doi.org/10.1029/2000WR900114

Yeh, T.-C. J., Srivastava, R., Guzman, A., & Harter, T. (1993). A numerical model for water flow and chemical transport in variably saturated porous media. *Ground Water*, *31*(4), 634–644. https://doi.org/10.1111/j.1745-6584.1993.tb00597.x

Yin, D., & Illman, W. A. (2009). Hydraulic tomography using temporal moments of drawdown recovery data: A laboratory sandbox study. *Water Resources Research*, *45*(1), W01502. https://doi.org/10.1029/2007WR006623

Zha, Y., Yeh, T.-C. J., Illman, W., Tanaka, T., Bruines, P., Onoe, H., et al. (2016). An application of hydraulic tomography to a large-scale fractured granite site. https://doi.org/10.1111/gwat.12421

Zhao, Z., & Illman, W. A. (2022). Improved high-resolution characterization of hydraulic conductivity through inverse modeling of HPT profiles and steady-state hydraulic tomography: Field and synthetic studies. *Journal of Hydrology*, *612*, 128124. https://doi.org/10.1016/j.jhydrol.2022.128124

Zheng, F., Chen, Z., & Zhang, J. (1999). A finite-difference time-domain method without the courant stability conditions. *IEEE Microwave and Guided Wave Letters*, *9*(11), 441–443. https://doi.org/10.1109/75.808026

Zhou, W. (2008). *Dynamic simulation of groundwater in handan plain area*. Hebei University of Engineering. (in Chinese).

Zhu, J., & Yeh, T.-C. J. (2006). Analysis of hydraulic tomography using temporal moments of drawdown recovery data. *Water Resources Research*, *42*(2), W02403. https://doi.org/10.1029/2005WR004309